



Sintering kinetics of Ni₂FeSb powder alloys produced by mechanical milling

F. ALVARADO-HERNÁNDEZ¹, O. JIMÉNEZ², G. GONZÁLEZ-CASTAÑEDA¹, V. BALTAZAR-HERNÁNDEZ¹,
J. CABEZAS-VILLA³, M. ALBITER³, H. VERGARA-HERNÁNDEZ⁴, L. OLMOS³

1. Unidad Académica de Ingeniería I, Universidad Autónoma de Zacatecas,
Jardín Juárez 147 Centro Histórico, Zacatecas, Zacatecas, C. P. 98000, México;

2. Departamento de Ingeniería de Proyectos, CUCEI, Universidad de Guadalajara,
Blvd. Marcelino García Barragán 1421, Olímpica, Guadalajara, Jalisco, C. P. 44430, Mexico;

3. INICIT, Universidad Michoacana de San Nicolás de Hidalgo,
Fco. J. Mujica S/N, C.U., Morelia, Michoacán, C. P. 58060, México;

4. División de Estudios de Posgrado e Investigación, TecNM/Instituto Tecnológico de Morelia,
Av. Tecnológico # 1500, Colonia Lomas de Santiaguito, Morelia, Michoacán, C. P. 58120, México

Received 21 September 2015; accepted 28 February 2016

Abstract: A ternary Ni₂FeSb shape memory alloy was fabricated by powder metallurgy route. Sintering kinetics was estimated from dilatometry tests; whereas the microstructure and morphology of the powder and consolidated bulk samples were evaluated by XRD and SEM, respectively. Microhardness tests were performed on the surface of sintered samples. The results indicated that milling time has an effect on the shape and particle size as well as the homogeneity of the crystalline structures of the powders. Samples with longer milling time presented higher relative densities, better distribution of the elements on the alloy as well as the L2₁ and martensite phases, which will give the shape memory effect. The estimated activation energy values ranged from 109 to 282 kJ/mol at temperatures between 750 and 1273 K, indicating that sintering is controlled mainly by volume diffusion. Microhardness was improved by increasing the milling time and the heating rate.

Key words: Ni-based shape memory alloy; mechanical milling; solid state sintering; microhardness

1 Introduction

Ferromagnetic shape memory alloys (FSMAs) have recently attracted the interest of researchers, given their unique ability to produce large deformation induced by a magnetic field (MFIS) [1–6]. These alloys are also well known because they exhibit a short response time and high reversible deformation capacity followed by a high stability of the ferromagnetic modulated martensite structure, high magneto-crystalline anisotropy (MCA) and high capacity of magnetization [1,2]. These alloys also exhibit a thermally induced shape memory effect [7,8]. The FSMAs are commonly prepared by electric arc melting in addition to other conventional processes [9,10]. Processing of those alloys is a difficult task since difficulties arise due to differences in melting points of the component elements [11]. Some investigations showed that the mechanical alloying

process is an attractive alternative in order to produce alloys of elements that are not easy to work by conventional means and, sometimes, even impossible to prepare. For example, when elements cannot be mixed under equilibrium conditions [12,13], different processing techniques have been used to produce powders including spark erosion, which is a rapid solidification process [14,15]. Also, nano-crystalline alloys and intermetallic compounds were successfully produced via mechanical alloying by different authors [16–19]. Additionally, it has been found that metastable phases, such as supersaturated solid solutions, intermediate quasi-crystalline phases and amorphous alloys, can be synthesized by mechanical alloying. Furthermore, nanostructures with a grain size of a few nanometers (below 100 nm) can also be produced by this method [12,13]. Different Ni-based shape memory alloys have been produced by sintering [20–22]. In the case of the Ni–Ti alloy, it has been largely studied by

conventional sintering where the diffusion mechanisms were established to occur during sintering [20,23]. Other alloys like Ni–Mn–Ga [24], Cu–Al–Ni [25,26] and NiCoMnSn [27] were produced by some other methods like spark plasma sintering (SPS). Different research groups concluded that mechanical properties were improved and the martensitic transformation temperatures increased against those produced by casting. Antimony is an element that has gained popularity in alloys such as Ni–Mn–Sb with different compositions and fabricated by conventional means like induction melting and electric arc furnace [17–19]. However, the use of this element in Ni–Fe-based alloys as a third element has not been reported. In this research, the selection of Sb was done aiming to produce, characterize and obtain a Sb-containing potential ferromagnetic shape memory alloy (Ni_2FeSb) by mechanical alloying technique.

2 Experimental

Initially, high purity (>99.9%) powders of Ni, Fe and Sb (Goodfellow) with particles size between 70 and 90 μm were mixed with the stoichiometric volume fraction of each element in order to obtain an alloy of $\text{Ni}_{50}\text{Fe}_{25}\text{Sb}_{25}$. The mixture was introduced into an alumina container with two alumina balls of 12.25 mm in diameter in a high energy ball mill SPEX 8000M at 1725 r/min. Then, the resulting powders were milled at two different milling time, 12 and 24 h, respectively. The milling time was determined from previous studies. GHOTBI VARZANEH et al [28] found the L_{21} structure in a $\text{Ni}_{47}\text{Mn}_{40}\text{Sn}_{13}$ alloy fabricated from elementary powders for a milling time of 20 h. The mixture crystalline structure was assessed by X-ray diffraction (XRD) using a D8 Bruker diffractometer, whereas the shape and size of particles were observed with a Tescan field emission scanning electron microscope (FESEM). Then, powders were introduced into an 8 mm diameter stainless steel die and uniaxially pressed by means of an Instron 1150 universal machine. In order to produce compacts of 4 mm in height, the maximal pressure used was 500 MPa without any binder. Finally, compacts were sintered in a vertical dilatometer Linseis L75 at 1273 K under an inert atmosphere of Ar. In order to estimate the kinetics parameters during sintering, three different heating rates were used, being 5, 15 and 25 $^{\circ}\text{C}/\text{min}$. The sintered compacts were cut, and then the surface of the sample was metallographically prepared by grinding and polishing with SiC papers and alumina powders respectively. The microstructure of sintered samples was also observed through scanning electron microscopy. The crystalline structure was determined by XRD

experiments; while microhardness tests over the polished surface were carried out with a Mitutoyo microhardness tester at a load of 200 g.

3 Results and discussion

3.1 Powders and green conformed

The shape and size of milled powders milled for 12 and 24 h are shown in Fig. 1. It can be noticed that powders milled for 24 h (Fig. 1(a)) present a wide particle size distribution since not only particles smaller

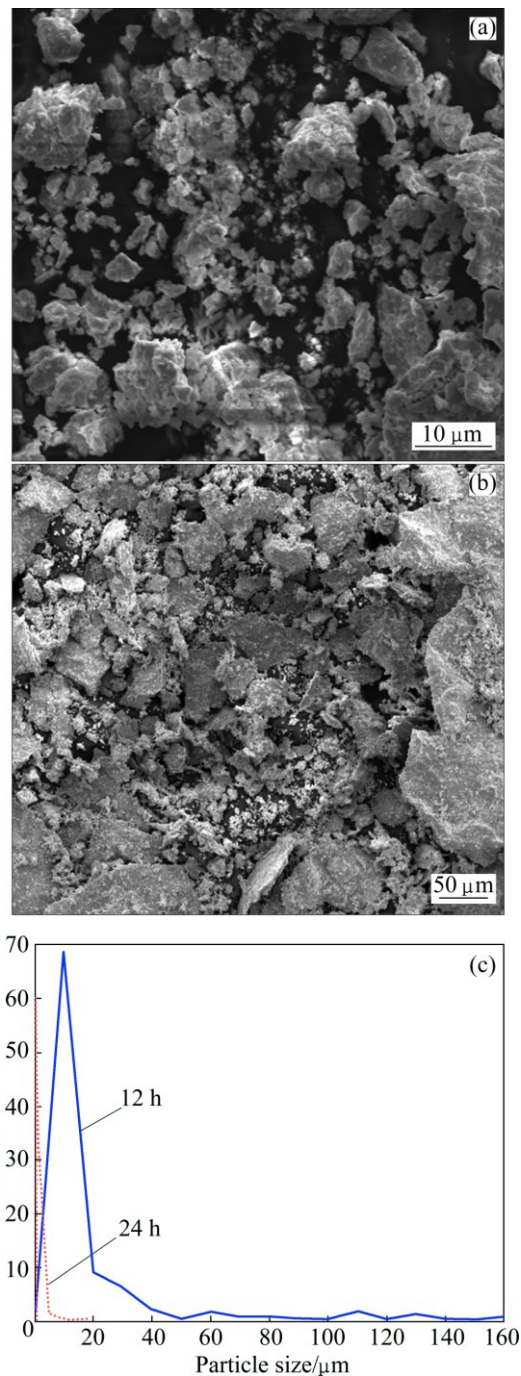


Fig. 1 Microstructures of Ni–Fe–Sb powder alloy obtained after mechanical milling for 24 h (a), 12 h (b) and particle size distribution (c)

than 1 μm can be easily observed, but also particles larger than 20 μm are seen after milling. On the other hand, when the milling time was 12 h (Fig. 1(b)), particles larger than 100 μm are found, but most of particles are inferior to 40 μm in diameter. The particle size distribution was determined by measuring 1000 particles from different SEM images. In order to obtain a representative value, the Ferret's diameter was measured to determine the particle size (Fig. 1(c)). The d_{50} obtained for 24 h milling was 1 μm , which is four times smaller than that measured for 12 h of milling. We can also notice that the particle size distribution is narrower when longer milling time is used, for such case the span value $((d_{90}-d_{10})/d_{50})$ was calculated and it was found that the value is 10 times larger for 12 h of milling; 17 and 1.8 for both 12 and 24 h, respectively. A better morphology uniformity and particle size distribution are obtained when 24 h of milling is used and it will certainly help during the sintering stage.

Figure 2 shows the XRD patterns of the powders milled for 12 and 24 h, which indicates that the processing time of 12 h results in a heterogeneous mixture. It can be noticed that the diffraction peaks correspond to the individual constituent elements before alloying and only trace (small quantity) of a Ni–Sb binary phase is seen according to the well-known phase

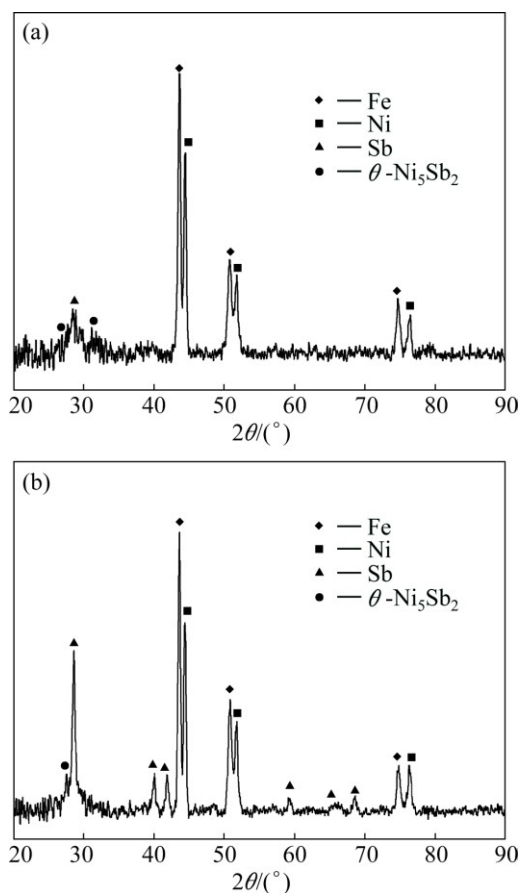


Fig. 2 XRD patterns of powders milled for 24 h (a) and 12 h (b)

diagram of Ni–Sb. These results are most probably a consequence of the relatively short time of the mechanical alloying process. Despite increasing the milling process time to 24 h, there is not a significant improvement in the alloy mixing since the characteristic peaks of the individual elements initially added are still detected. However, the peak seen at 2θ of 29° corresponding to Sb element shows less intensity and peaks previously observed at 2θ of 39° and 41° seem to be suppressed. Additionally, more peaks coinciding with the Ni–Sb phase are found at 2θ of 27° and 32° .

The behavior of powders under compression is presented in Fig. 3. It can be seen that powders milled for 12 h reach higher green relative densities than those milled for 24 h. This agrees with the observation of the particle size, since smaller-particle powders have a lower rearrangement during the compression because it is difficult to eliminate agglomerates during this process. It is also seen that after particles' rearrangement, the stress increases exponentially which is an indicative of a brittle behavior seen in both powders, as it is expected for this alloy.

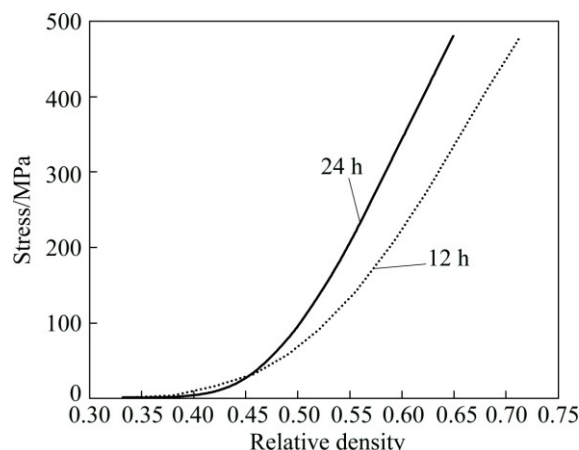


Fig. 3 Stress as function of relative density during whole test of compaction for both powders

3.2 Sintering behavior

Sintering behavior was studied by means of dilatometry experiments using three different heating rates (5, 15 and 25 $^\circ\text{C}/\text{min}$) to attain 1273 K, which was selected as the sintering temperature. The shrinkage during the whole thermal cycle for all samples is shown in Fig. 4. It is observed that at around 500 K, a small contraction happens corresponding to the stress relief generated during milling. Then, samples milled for 12 h have a strong swelling at around 600 K, which is related to the phase transformation. This phenomenon is less pronounced in samples milled for 24 h. It is assumed that a longer milling time might lead to a better formation of the alloy. For this case, it is believed that by reducing the heating rate, the swelling is reduced because the

transformation has enough time to evolve from one phase to another. Passing this, the sintering is activated at around 900 K. This is indicated by a continuous shrinkage until reaching the sintering plateau at 1273 K. During the cooling stage, no reverse transformation is detected. At the end, we can notice that the shrinkage is larger for samples milled for 24 h. The shrinkage achieved during the whole thermal cycle is increased by 13% when the lower heating rate is used in comparison to higher heating rate for the two kinds of powders.

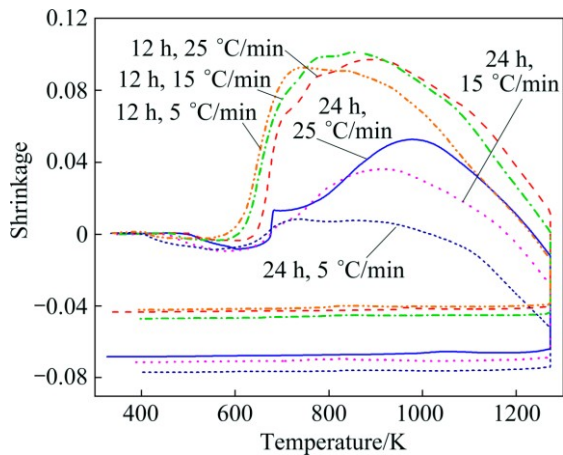


Fig. 4 Shrinkage as function of temperature during whole sintering cycle at different heating rates for both powders

In order to compare the shrinkage during the sintering plateau, we depicted it as a function of the isothermal time in Fig. 5(a). It is observed that larger shrinkage is achieved as the heating rate increases for both powders. These results are expected because at lower heating rates, most of the shrinkages occur during the heating stage, thereby giving enough time for the samples to shrink since the activation of sintering starts at around 900 K for all samples. It is also noticed that a significant shrinkage reaches by the compacts produced with powders milled for 12 h. This is mainly because the sintering is slower due to the larger particles; then the maximal shrinkage at the same temperature reaches during the isothermal time instead of happening at the heating stage. For all the heating rates used shown in Fig. 5(b), the densification rate confirms that sintering is slower for powders milled for 12 h than for those milled for 24 h. It is also noticed that the densification rate at the same relative density is higher when the heating rate is reduced. This is because the samples sintered with the lower heating rate reach higher values of relative densities at the beginning of the sintering plateau. Figure 5(b) shows that the higher relative densities occur at the end of isothermal sintering when the lower heating rate is used. This is mainly because the relative density, at the beginning of the sintering plateau, is 13% higher for samples heated at 5 °C/min. On the other hand, a

larger densification is achieved at 1273 K when lower heating rates are used, which equilibrates the relative density reached, being approximately 4% higher for samples sintered at lower heating rates, for the two kinds of powders. The ratio of the axial strain to radial strain after sintering was calculated for all samples in order to evaluate the isotropy during densification. It was found that samples with powders milled for 24 h presented a ratio being around 1; meanwhile, samples composed of powders milled for 12 h have a value of 2, no matter what heating rate was used. This anisotropy can be attributed to the shape of particles because larger particles could be oriented in the perpendicular direction to compaction, hence, fewer number of contacts between particles will reduce the densification during sintering.

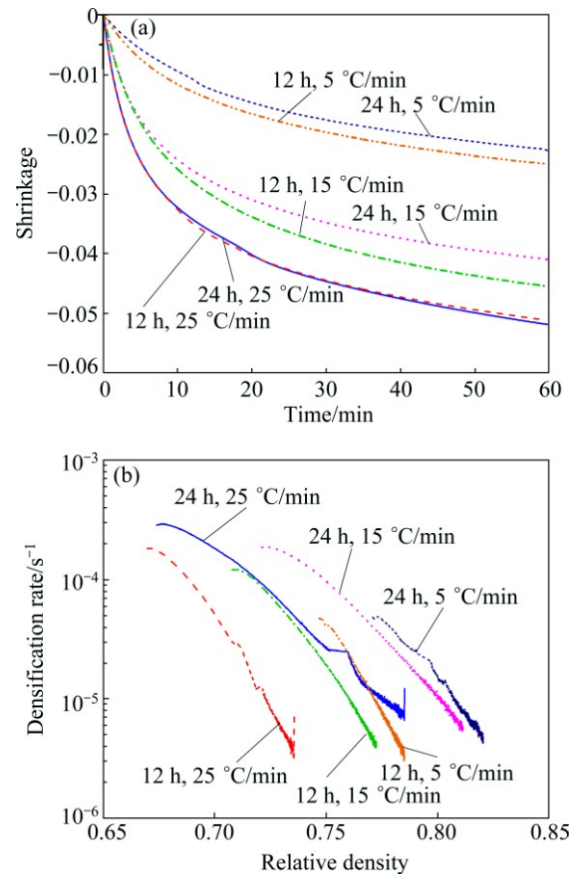


Fig. 5 Axial shrinkage as function of time during isothermal sintering (a) and densification rate as function of relative density (b) for samples sintered at different heating rates

In order to compare the densification $((D-D_0)/D_0)$ reached during different thermal cycles, a plot of the densification as a function of the heating rate is plotted in Fig. 6. It is observed that more densification is achieved when lower heating rate is used, for the two kinds of powders. However, samples with powders milled for 24 h achieve 2.5 times more densification during sintering in spite of green relative density after compaction is lower. That is caused by the particle size

of the obtained powders after milling, which results in four times smaller than that milled for only 12 h.

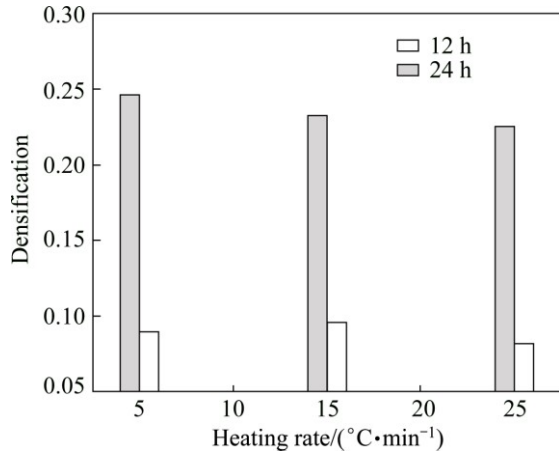


Fig. 6 Densification achieved during whole sintering cycle as function of heating rate

3.3 Estimation of activation energy

The activation energy (Q) for the two kinds of powders milled for 12 and 24 h, was estimated using the constant heating rate method proposed by WANG and RAJ [29] (see Eq. (1)), which is valid for the initial and intermediate stages of sintering.

$$\ln\left(Tc\left(\frac{dY}{dT}\right)\right) = -\frac{Q}{RT} + \ln k_0 - \ln G^{\alpha k} + \ln f(Y) \quad (1)$$

where Y is the linear shrinkage, $Y=dL/L_0$, L_0 is the initial length, T is the thermodynamic temperature, c is the constant heating rate, $c=dT/dt$, t is the time, G is the grain size, k is Boltzmann's constant, α and k_0 are material constants, $f(Y)$ is a function of density, Q is the sintering activation energy, and R is the mole gas constant.

To estimate the value of Q , we calculated the left part of Eq. (1), and we depicted the points as a function of the inverse of the temperature at which a certain value of relative density is obtained (Fig. 7). Since the heating rate is different, the temperature to reach the same relative density will be different too. Then, we calculated the linear fit for the data at the same value of relative density and we obtained the value of Q/R from the slope of that fit. Finally, Q was estimated by using the value of $R=8.3145$ J/(K·mol). The calculated values of Q for the two kinds of powders at different relative densities are listed in Table 1. We observed that higher Q values were found for smaller particle powders except for the 67% relative density where a higher Q was found for the larger-particle powders. The values obtained for samples with milling time of 24 h indicated that the volume diffusion drives the sintering during early stages since the Q values reported for Ni ranged from 136 to 276 kJ/mol [30–32] and then, Q value decreased possibly to be driven by the grain boundary diffusion

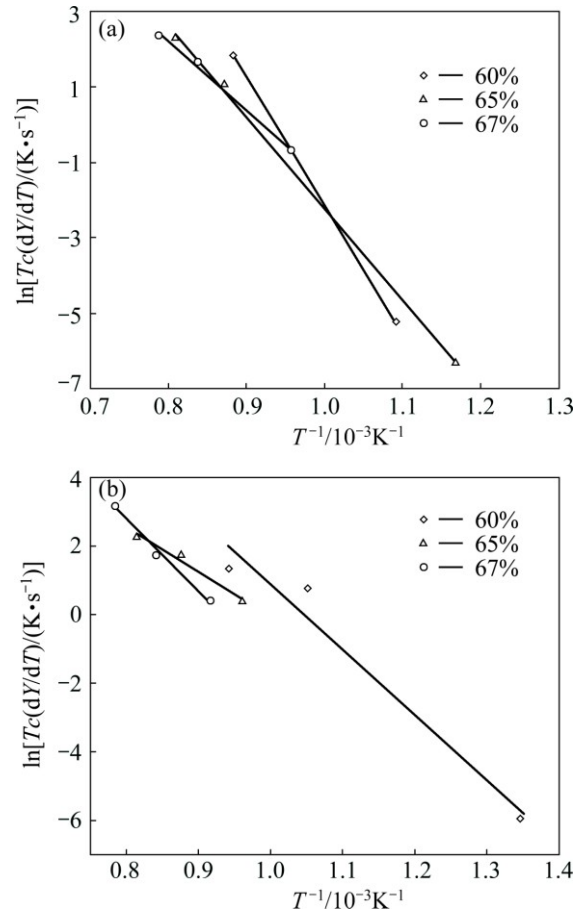


Fig. 7 Plots to estimate activation energy from different heating rates for both powders milled for 24 h (a) and 12 h (b) with different relative densities

Table 1 Sintering activation energies at different densities and temperature ranges for powders of Ni–Fe–Sn milled for 24 and 12 h

Sample	Instantaneous relative density/%	Temperature range/K	Sintering activation energy/(kJ·mol ⁻¹)
Powders milled for 24 h	60	915–1130	282
	65	860–1200	201
	67	1040–1273	151
Powders milled for 12 h	60	750–1050	159
	65	1040–1200	109
	67	1090–1273	173

which was reported to be 108 kJ/mol [30]. The reduction of the apparent activation energy was observed by LUKE [33] during nickel powder sintering by SPS technique and by SHAO et al [34] in conventional sintering of processed alumina using the same method to estimate the activation energy. The authors suggested that at low density, densification only occurs by volume diffusion and that as the density increases, the other diffusion mechanisms, especially grain boundary

diffusion, play a more important role in densification and their contribution is reflected by the decrease in activation energy. Those values are approximately 286 kJ/mol and compared for the self-diffusion of nickel determined by other means [31]. On the other hand, the 12 h milled powders seem to be mainly controlled by the grain boundary diffusion mechanism. Although, ELLIOT and MUNIR [32] found an activation energy of 136 kJ/mol for spheres sintering onto plate of nickel, and they concluded that volume diffusion was the main sintering mechanism. The relatively high activation energy values indicate that no diffusion of nickel in liquid state is present as it was reported by other authors [20,35,36]. These results indicate that the particle size has a strong influence on the sintering behavior; nevertheless, the sintering can also be affected by the phase transformation that occurs at around 600 K.

3.4 Microstructural analysis

Internal microstructures of powders after sintering were observed by FESEM and shown in Figs. 8 and 9. From the images, three zones are observed. A black one which corresponds to the pores, dark and light grey phases are related to the alloy. In the case of 24 h milled powders, lower porosity was found with more regular shape than that obtained for the 12 h milled powders.

Neither of the micrographs shows the original shape of particles, indicating a very good diffusion during sintering. The main difference noticed is the lamellar shape of the dark grey phase in the 12 h milled powders (Fig. 9) contrary to a random distribution of the same phase presented in powders milled for 24 h. The lamellar microstructure can be attributed to the initial particles shape, which looked mostly like flakes and were different from the microstructure of powders milled for 24 h that had mostly an irregular morphology.

In order to elucidate the phase distribution over the surface of the samples, an EDS elemental mapping of Ni, Fe and Sb was performed for the alloy (Fig. 10). This figure presents the elemental distribution for samples sintered at 1273 K with a heating rate of 5 °C/min for two milling time. It is observed that Ni is homogeneously distributed over the whole sample. Fe is mainly distributed on the dark grey phase and poorly placed over the rest of the surface sample. On the contrary, Sb is mainly present in the light grey phase and poorly distributed in the other phase.

Figure 11 shows the XRD patterns of the samples sintered for 1 h at 1273 K for two milling time. For the 12 h sample, it is noticeable for the presence of binary compounds known as Ni–Sb and Fe–Ni in different compositions. Also, a few of peaks coinciding with the

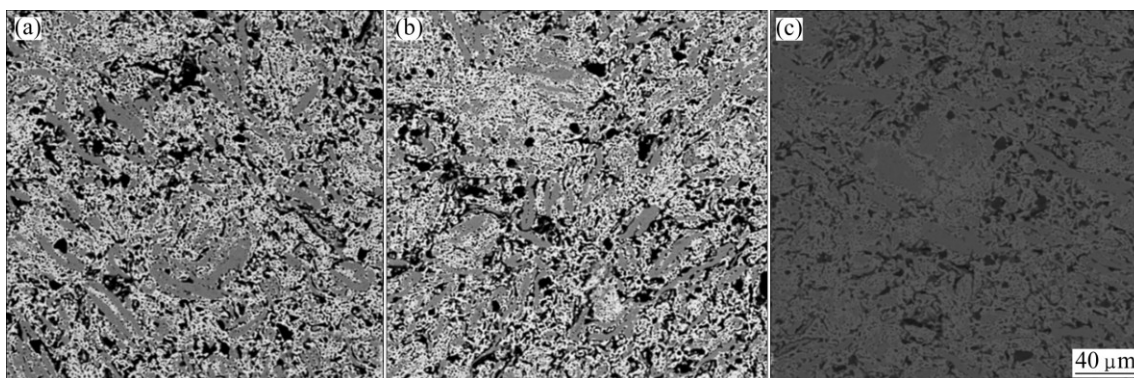


Fig. 8 FESEM images of powders milled for 24 h and sintered at 1273 K with different heating rates: (a) 25 °C/min; (b) 15 °C/min; (c) 5 °C/min

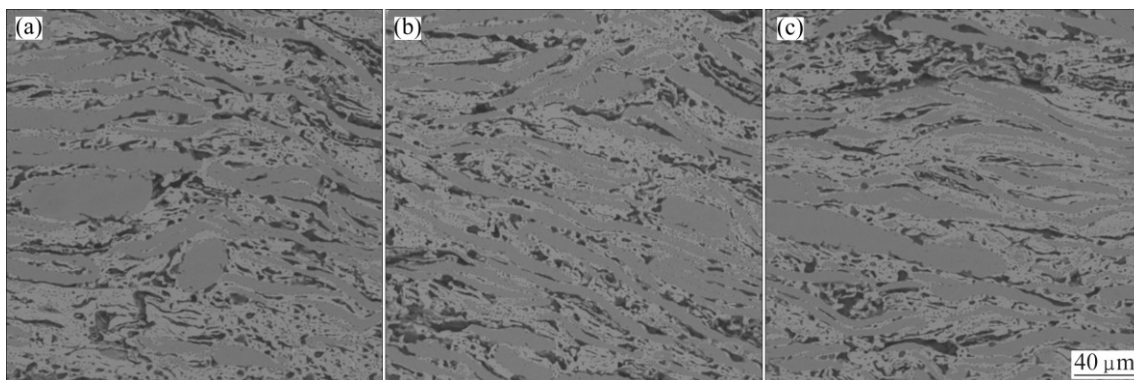


Fig. 9 FESEM images of powders milled for 12 h and sintered at 1273 K with different heating rates: (a) 25 °C/min; (b) 15 °C/min; (c) 5 °C/min

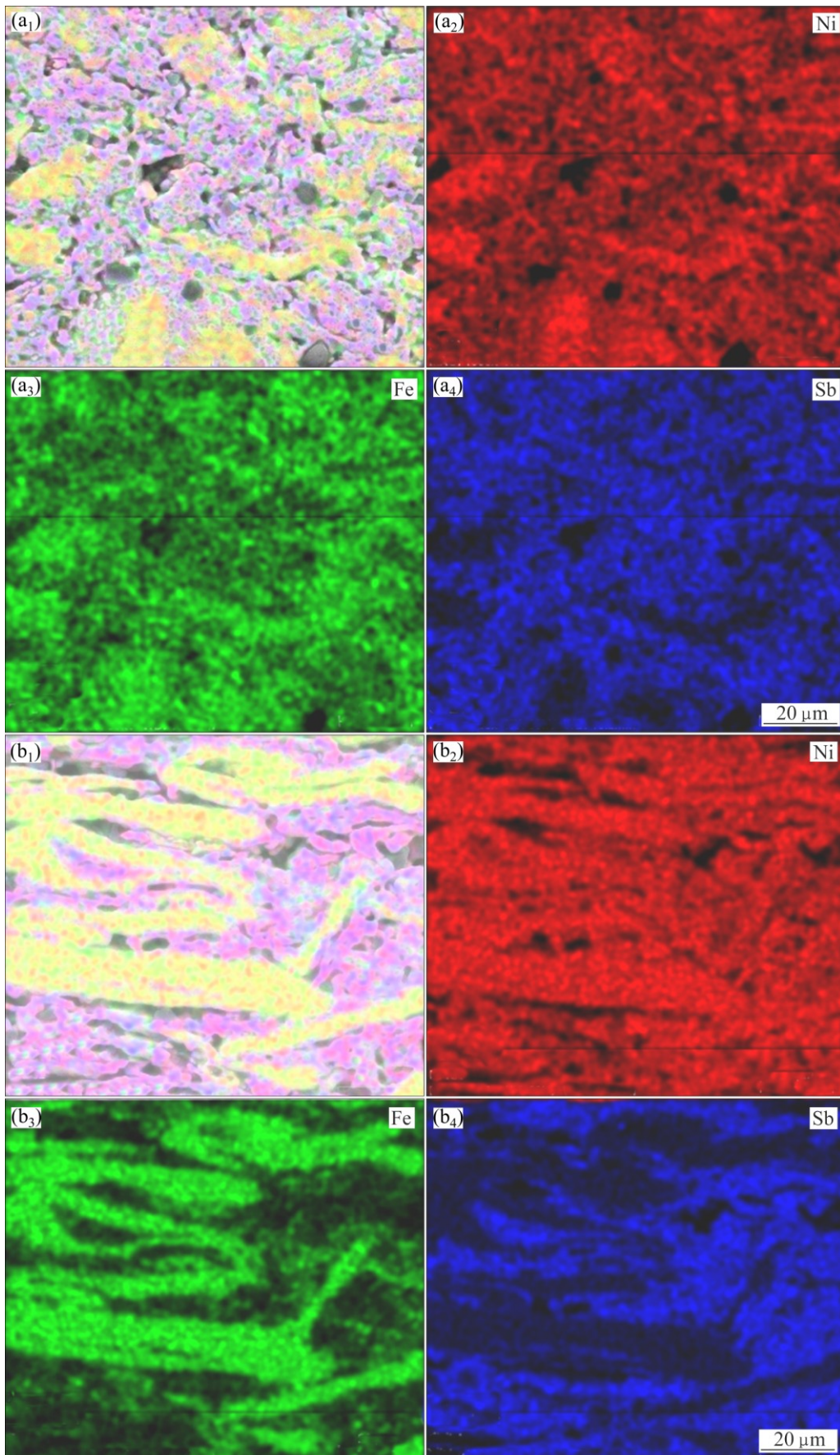


Fig. 10 EDS elemental mapping of Ni-Fe-Sb samples sintered at 1273 K with heating rate 5 °C/min for 24 h (a₁-a₄) and 12 h (b₁-b₄)

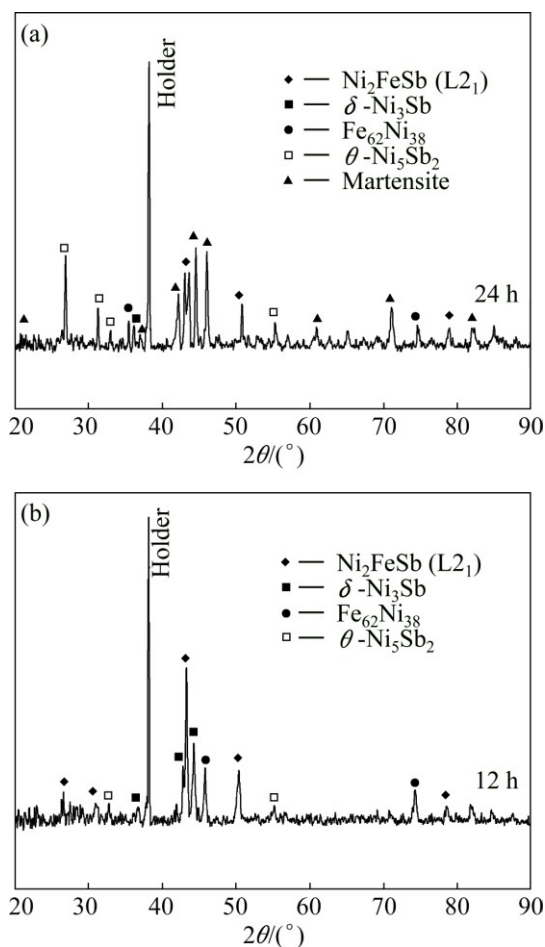


Fig. 11 XRD patterns of Ni–Fe–Sn sintered samples

ternary compound of Ni_2FeSb can be noticed, which is desirable for this alloy. The diffraction peaks (220) and (311) approximately at 2θ of 43° and 51° respectively and the average lattice parameter (5.94 \AA) calculated from the XRD patterns are in agreement with a $L2_1$ structure for this type of structures and alloys [37,38]. The appearance of both peaks confirms a high probability of the $L2_1$ structure as reported by BARMAN et al [37]. It should be pointed out that no elements segregated individually, only different phases with different compositions were observed, which may be due to the nature of the alloy formation.

All the phases detected for 12 h milling sample can also be observed for the 24 h milling sample, whereas the lattice parameter calculated for this sample resulted in quite similar, i.e., 5.93 \AA . Another feature that should be highlighted is the appearance of a peak, most likely corresponding to martensite, which has been previously reported by KHALID AHMAD and ZAMEER ABBAS [38] and SAHOO et al [39] for this type of alloys. This presumable martensite peak is located at 2θ of approximately 44° and it is also consistent with the results obtained by other researchers in similar studies [40].

3.5 Microhardness

Figure 12 shows the microhardness values obtained for different sintered samples as a function of the heating rate. It was found that microhardness increased generally for 24 h milling time in comparison to its 12 h milling time counterpart. For the first two heating rates (5 and $15^\circ\text{C}/\text{min}$), the microhardness was about 25% higher for longer milling time. For the case when the highest heating rate was used ($25^\circ\text{C}/\text{min}$), an exponential increment behavior is observed for 24 h milling sample, reaching an increment of about 65% in comparison to that of 12 h milling sample. This is because as the heating rate increases, the grain is impeded to grow. At higher heating rates, some of the stored energy could be preserved within the sample, leading to a smaller grain size rather than the development of large ones. The absence of any enhancement of microhardness for 12 h milling samples could be understood by that under this condition powders are large enough and the effect of grain growth during the thermal cycle is meaningless.

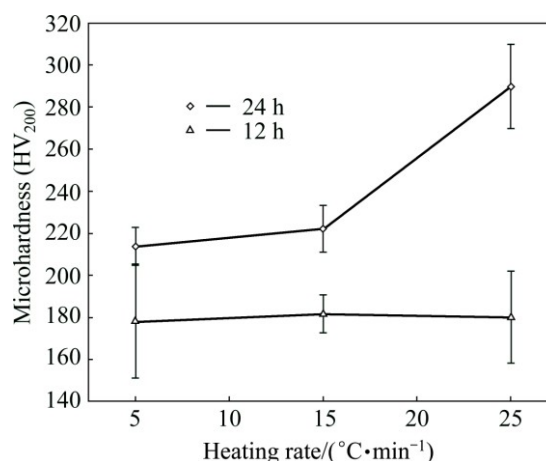


Fig. 12 Microhardness of sintered Ni–Fe–Sb alloys as function of heating rate of sintered samples

4 Conclusions

A Ni_2FeSb alloy was obtained by the powder metallurgy route. The milling time affected the alloy homogeneity and the particle size distribution of the powders, modified the sintering behavior of powders and the final crystalline structures. After sintering for the samples with 12 h of milling, the $L2_1$ phase was not found, which provides the shape memory properties. On the other hand, samples with milling time of 24 h showed the $L2_1$ and martensite phases coexisting at room temperature. This indicated the capability for the memory shape behavior. The activation energy indicated that volume diffusion is the predominant mechanism for early sintering and as the sintering advances, several mechanisms become active, and the grain boundary diffusion is the most predominant. Microhardness was

improved for the samples with milling time of 24 h and the best results were obtained when the highest heating rate was used.

Acknowledgement

The authors want to thank PROMEP/ 103.5/13/6992 and the CIC of the UMSNH for the financial support and facilities to develop this work as well as CONACYT under the project CB-2011-167111.

References

- [1] ULLAKKO K, HUANG J K, KANTNER C, O'HANDLEY R C, KOKORIN V V. Large magnetic-field-induced strains in Ni₂MnGa single crystals [J]. *Applied Physics Letters*, 1996, 69: 1966–1968.
- [2] O'HANDLEY R C. Model for strain and magnetization in magnetic shape-memory alloys [J]. *Journal of Applied Physics*, 1998, 83: 3263–3270.
- [3] SÖDERBERG O, AALTIO I, GE Y, HECZKO O, HANNULA S P. Ni–Mn–Ga multifunctional compounds [J]. *Materials Science and Engineering A*, 2008, 481–482: 80–85.
- [4] PONS J, CESARI E, SEGUÍ C, MASDEU F, SANTAMARTA R. Ferromagnetic shape memory alloys: Alternatives to Ni–Mn–Ga [J]. *Materials Science and Engineering A*, 2008, 481–482: 57–65.
- [5] XU G F, YIN Z M, MOU S, LUO F, OIKAWA K. Martensitic and magnetic transformation of Co₄₁Ni₃₂Al₂₄Sb₃ and Co₄₁Ni₃₂Al₂₇ alloys [J]. *Transactions of Nonferrous Metals Society of China*, 2006, 16: 776–782.
- [6] CAO J M, TAN C L, TIAN X H, LI Q C, GUO E J, WANG L P, CAO Y J. Effect of Co substitution on magnetic properties of Ni–Mn–Sn magnetic shape memory alloys [J]. *Transactions of Nonferrous Metals Society of China*, 2014, 24: 1053–1057.
- [7] CHERNENKO V A. Compositional instability of β -phase in Ni–Mn–Ga alloys [J]. *Scripta Materialia*, 1999, 40: 523–527.
- [8] PLANES A, MAÑOSA L L, MOYA X, KRENKE T, ACET M, WASSERMANN E F. Magnetocaloric effect in Heusler shape-memory alloys [J]. *Journal of Magnetism and Magnetic Materials*, 2007, 310: 2767–2769.
- [9] NAYAK A K, RAMA R N, SURESH K, NIGAM A. Magneto-thermal and magneto-transport behavior around the martensitic transition in Ni_{50-x}CoxMn₄₀Sb₁₀ (x=9, 9.5) Heusler alloys [J]. *Journal of Alloys and Compounds*, 2010, 499: 140–143.
- [10] WU D, XUE S, FRENZEL J, EGGELER G, ZHAI Q, ZHENG H. Atomic ordering effect in Ni₅₀Mn₃₇Sn₁₃ magnetocaloric ribbons [J]. *Materials Science and Engineering A*, 2012, 534: 568–572.
- [11] SCHLAGEL D L, WU Y L, ZHANG W, LOGRASSO T A. Chemical segregation during bulk single crystal preparation of Ni–Mn–Ga ferromagnetic shape memory alloys [J]. *Journal of Alloys and Compounds*, 2000, 312: 77–85.
- [12] KOCH C C. *Mechanical milling and alloying* [M]. Weinheim: Wiley-VCH, 1991: 193–245.
- [13] MURTY B S, RANGANATHAN S. Novel materials synthesis by mechanical alloying/milling [J]. *International Materials Reviews*, 1998, 43: 101–141.
- [14] TANG Y J, SOLOMON V C, SMITH D J, HARPER H, BERKOWITZ A E. Magnetocaloric effect in NiMnGa particles produced by spark erosion [J]. *Journal of Applied Physics*, 2005, 97: 10M309.
- [15] BERKOWITZ A E, WALTER J L. Spark erosion: A method for producing rapidly quenched fine powders [J]. *Journal of Materials Research*, 1987, 2: 277–288.
- [16] ZHOU L Z, GUO J T, FAN G J. Synthesis of NiAl–TiC nanocomposite by mechanical alloying elemental powders [J]. *Materials Science and Engineering A*, 1998, 256: 103–108.
- [17] SMITH T R, VECCHIO K S. Synthesis and mechanical properties of nanoscale mechanically-milled NiAl [J]. *Nanostructured Materials*, 1995, 5: 11–23.
- [18] PYO S G, KIM N J, NASH P. Transmission electron microscopy characterization of mechanically alloyed NiAl powder and hot-pressed product [J]. *Materials Science and Engineering A*, 1994, 181–182: 1169–1173.
- [19] SMITH T R. Synthesis and mechanical properties of nano-scale NiAl and NiAl/Al₂O₃ composites [C]//*Proceedings of the Materials Research Society Symposium*. Ambridge, 1994: 219.
- [20] PANIGRAHI B B, GODKHINDI M M. Dilatometric sintering study of Ti–50Ni elemental powders [J]. *Intermetallics*, 2006, 14: 130–135.
- [21] JIANG H J, KE C B, CAO S S, MA X, ZHANG X P. Phase transformation and damping behavior of lightweight porous TiNiCu alloys fabricated by powder metallurgy process [J]. *Transactions of Nonferrous Metals Society of China*, 2013, 23: 2029–2036.
- [22] YUAN Y B, WANG Z W, ZHENG R X, HAO X N, AMEYAMA K, MA C L. Effect of mechanical alloying and sintering process on microstructure and mechanical properties of Al–Ni–Y–Co–La alloy [J]. *Transactions of Nonferrous Metals Society of China*, 2014, 24: 2251–2257.
- [23] GREEN S M, GRANT D M, KELLY N R. Powder metallurgical processing of Ni–Ti shape memory alloy [J]. *Powder Metallurgy*, 1997, 40: 43–47.
- [24] TIAN X H, SUI J H, ZHANG X, ZHENG X H, CAI W. Grain size effect on martensitic transformation, mechanical and magnetic properties of Ni–Mn–Ga alloy fabricated by spark plasma sintering, [J]. *Journal of Alloys Compounds*, 2012, 514: 210–213.
- [25] XIAO Z, LI Z, FANG M, LUO M, GONG S, TANG N. Structure evolution of Cu-based shape memory powder during mechanical alloying [J]. *Transactions of Nonferrous Metals Society of China*, 2007, 17: 1422–1427.
- [26] PORTIER R A, OCHIN P, PASKO A, MONASTYRSKY G E, GILCHUK A V, KOLOMYTSEV V I, KOVAL Y N. Spark plasma sintering of Cu–Al–Ni shape memory alloy [J]. *Journal of Alloys Compounds*, 2013, 577: 472–477.
- [27] ITO K, ITO W, UMETSU R Y, TAJIMA S, KAWAURA H, KAINUMA R, ISHIDA K. Metamagnetic shape memory effect in polycrystalline NiCoMnSn alloy fabricated by spark plasma sintering [J]. *Scripta Materialia*, 2009, 61: 504–507.
- [28] GHOTBI VARZANEH A, KAMELI P, KARIMZADEH F, ASLIBEIKI B, VARVARO G, SALAMATI H. Magnetocaloric effect in Ni₄₇Mn₄₀Sn₁₃ alloy prepared by mechanical alloying [J]. *Journal of Alloys and Compounds*, 2014, 598: 6–10.
- [29] WANG J, RAJ R. Estimate of the activation energies for boundary diffusion from rate-controlled sintering of pure alumina, and alumina doped with zirconia or titania [J]. *Journal of the American Ceramic Society*, 1990, 73: 1172–1175.
- [30] GERMAN R M. *Sintering theory and practice* [M]. New Jersey: Wiley, 1996.
- [31] HUFFMAN R E, PIKUS F W, WARD R A. Self-diffusion in solid nickel [J]. *Transactions of the Metallurgical Society of AIME*, 1956, 206: 483–486.
- [32] ELLIOT A G, MUNIR Z A. The sintering of nickel/aluminium spheres to nickel plates [J]. *Journal of Materials Science*, 1968, 3: 150–157.
- [33] LUKE M T. *Microstructural evolution of nickel during spark plasma sintering* [D]. Idaho: Boise State University, 2010: 81.
- [34] SHAO W Q, CHEN S O, LI D, CAO H S, ZHANG Y C, ZHANG S S. Apparent activation energy for densification of α -Al₂O₃ powder at constant heating-rate sintering [J]. *Bulletin of Materials Science*, 2008, 31: 903–906.

- [35] DEMIRSKYI D, AGRAWAL D, RAGULYA A. Neck growth kinetics during microwave sintering of nickel powder [J]. *Journal of Alloys and Compounds*, 2011, 509: 1790–1795.
- [36] OLMOS L, ALVARADO-HERNÁNDEZ F, JIMÉNEZ O, VERGARA-HERNÁNDEZ H J, ARROYO ALBITER M, OCHOA-GAMBOA R A. Characterization of Ni_{53.5}-Fe_{19.5}-Ga₂₇-Ni_{53.5} ferromagnetic shape memory alloy produced by powder metallurgy [J]. *Revista de Metalurgia*, 2015, 51(2): 1–9.
- [37] BARMAN R, SINGH S K, KAUR D. Enhanced exchange bias in magnetron-sputtered Ni-Mn-Sb-Al ferromagnetic shape memory alloy thin films [J]. *Current Applied Physics*, 2014, 14: 1755–1759.
- [38] KHALID AHMAD F, ZAMEER ABBAS S. Characterization and properties of ferromagnetic shape memory alloys [J]. *Materials Characterization*, 2011, 62: 1134–1140.
- [39] SAHOO R, NAYAK A K, SURESH K G, NIGAM A K. Structural, magnetic, magnetocaloric and magnetotransport properties in Ge doped Ni-Mn-Sb Heusler alloys [J]. *Journal of Magnetism and Magnetic Materials*, 2012, 324: 1267–1271.
- [40] AKKERA H S, CHOUDHARY N, KAUR D. Martensitic phase transformations and magnetocaloric effect in Al co-sputtered Ni-Mn-Sb alloy thin films [J]. *Materials Science and Engineering B*, 2015, 198: 113–119.

机械球磨制备 Ni₂FeSb 合金的烧结动力学

F. ALVARADO-HERNÁNDEZ¹, O. JIMÉNEZ², G. GONZÁLEZ-CASTAÑEDA¹,
V. BALTAZAR-HERNÁNDEZ¹, J. CABEZAS-VILLA³, M. ALBITER³,
H. VERGARA-HERNÁNDEZ⁴, L. OLMOS³

1. Unidad Académica de Ingeniería I, Universidad Autónoma de Zacatecas,

Jardín Juárez 147 Centro Histórico, Zacatecas, Zacatecas, C. P. 98000, México;

2. Departamento de Ingeniería de Proyectos, CUCEI, Universidad de Guadalajara,

Blvd. Marcelino García Barragán 1421, Olímpica, Guadalajara, Jalisco, C. P. 44430, Mexico;

3. INICIT, Universidad Michoacana de San Nicolás de Hidalgo,

Fco. J. Mujica S/N, C.U., Morelia, Michoacán, C. P. 58060, México;

4. División de Estudios de Posgrado e Investigación, TecNM/Instituto Tecnológico de Morelia,

Av. Tecnológico # 1500, Colonia Lomas de Santiaguillo, Morelia, Michoacán, C. P. 58120, México

摘要: 采用粉末冶金工艺制备 Ni₂FeSb 三元形状记忆合金。利用膨胀实验研究合金的烧结动力学；采用 XRD 和 SEM 分别考察粉末样品和烧结样品的显微组织和形貌；测定烧结样品表面的显微硬度。结果表明：研磨时间对粉末样品的形状、晶粒尺寸和晶体结构的均匀性具有显著影响。经较长时间研磨的样品具有较高的相对密度和较均匀的元素分布，且为 L₂₁ 和马氏体相，这些性能使合金具有形状记忆功能。在温度为 750~1273 K 条件下，合金的激活能为 109~283 kJ/mol，这表明烧结过程主要由体积扩散控制。增加研磨时间和加热速率，合金的显微硬度得到提高。

关键词: Ni 基形状记忆合金；机械球磨；固态烧结；显微硬度

(Edited by Wei-ping CHEN)